



1 **Pseudotachylyte as field evidence for lower crustal earthquakes**
2 **during the intracontinental Petermann Orogeny (Musgrave**
3 **Block, Central Australia)**

4

5 Friedrich Hawemann¹, Neil S. Mancktelow¹, Sebastian Wex¹, Alfredo Camacho², Giorgio
6 Pennacconi³

7 ¹ Department of Earth Sciences, ETH Zurich, Sonneggstrasse 5, CH-8092 Zurich

8 ² Department of Geological Sciences, University of Manitoba, 125 Dysart Rd, Winnipeg, Manitoba, R3T 2N2 Canada.

9 ³ Department of Geosciences, University of Padova, Via Gradenigo 6, 35131 Padova, Italy


10 *Correspondence to:* Friedrich Hawemann (friedrich.hawemann@erdw.ethz.ch)



11 **Abstract.** Geophysical evidence for lower continental crustal earthquakes in almost all collisional orogens is in
12 conflict with the widely accepted notion that rocks, under high grade conditions, should flow rather than fracture.
13 Pseudotachylytes are remnants of frictional melts generated during seismic slip and can therefore be used as an
14 indicator of former seismogenic fault zones. The Fregon Domain in Central Australia, was deformed under dry sub-
15 eclogitic conditions during the intracontinental Petermann Orogeny (ca. 550 Ma) and contains abundant
16 pseudotachylyte. These pseudotachylytes are commonly foliated, recrystallized, and crosscut by other
17 pseudotachylytes, reflecting repeated generation during ongoing ductile deformation under generally dry conditions.
18 This interplay is interpreted as a cycle of seismic brittle failure and post- to inter seismic creep under dry lower crustal
19 conditions. Thermodynamic modelling of the pseudotachylyte bulk composition gives conditions of shearing of 600-
20 700 °C and 1.0-1.2 GPa, the same as in surrounding mylonites. We conclude that pseudotachylytes in the Fregon
21 Domain are a direct analogue of current seismicity in dry lower continental crust.

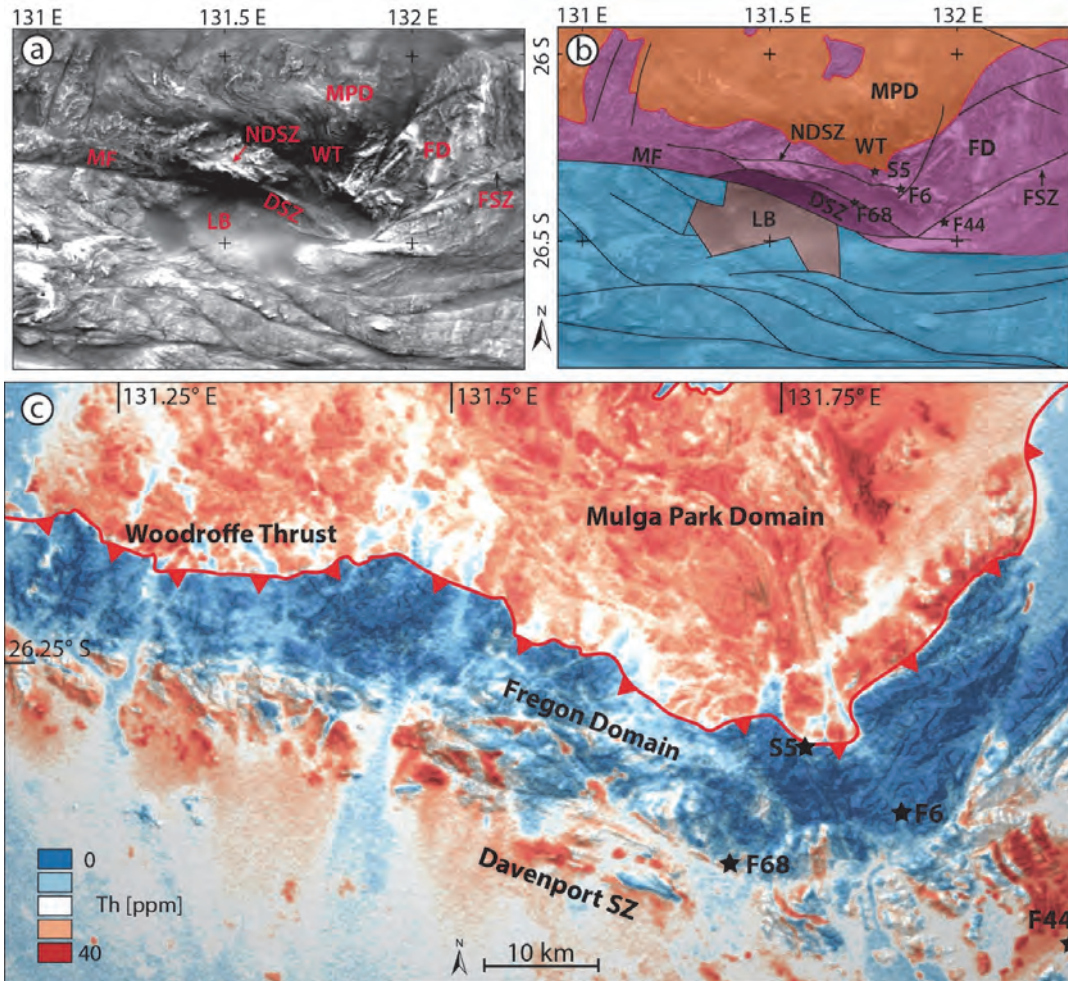
22 1 Introduction

23 Predicting the rheology of the Earth's crust is crucial for all geodynamic models over the whole range of length and
24 time scales from plate tectonics to seismic hazard estimation. In general, the main constraints on rock rheology are
25 derived from rock deformation experiments, where results at high strain rates and high temperatures are extrapolated
26 to natural conditions (e.g. Kohlstedt et al., 1995). The simplest assumption of competing brittle and viscous behaviour
27 at constant strain rate results in a typical “Christmas-tree” 1D representation of strength variation with depth (Goetze
28 and Evans, 1979). One basic form of the strength profile of the continental lithosphere is the so-called “jelly sandwich”
29 model, with a quartz- and feldspar-rich, wet, weak, and viscously flowing lower crust sandwiched between a strong
30 brittle upper crust and a dry, strong, brittle, upper mantle with olivine rheology (e.g. Burov and Watts, 2006; Jackson,
31 2002a). An alternative “crème brûlée” model considers a wet olivine rheology for the upper mantle, and therefore
32 limits all significant strength and seismicity to the upper crust (Burov and Watts, 2006; Jackson, 2002a). However, in
33 contradiction to such models that limit brittle deformation exclusively to the upper crust, seismicity is also recorded
34 in the lower crust in almost all collisional settings, e.g. the Alps (Deichmann and Rybach, 1989; Singer et al., 2014),
35 the Himalayas (Jackson, 2002b; Jackson et al., 2004), the Tien Shan (Xu et al., 2005), the central Indian shield (Rao
36 et al., 2002), and the North Island of New Zealand (Reyners et al., 2007).

37 The main factors governing rock rheology are temperature, strain rate, chemical composition and pore fluid pressure.
38 These parameters cannot be well constrained from seismic measurements. Consequently, direct observations from
39 field studies of exposed lower crustal sections are critical for understanding lower crustal rheology. Pseudotachylytes,
40 generally interpreted to represent frictional melt generated during seismic failure (McKenzie and Brune, 1972; Sibson,
41 1975), can be locally abundant in exposures of lower crust (Altenberger et al., 2011, ; Austrheim and Boundy,
42 1994; Clarke and Norman, 1993; Moecher and Steltenpohl, 2009, 2011; Pittarello et al., 2012). The metamorphic
43 conditions of these sections correspond to depths well below the usual brittle-ductile transition zone for crustal rocks
44 and thus the assumed lower limit for earthquake nucleation. Sibson (1980) reported mutually overprinting
45 pseudotachylytes and mylonites from the Outer Hebrides Thrust (NW Scotland) and similar observations were made



81 around 550 Ma (Camacho et al., 1997), all of which are associated with abundant pseudotachylytes. The Fregon
82 Subdomain was then juxtaposed against former mid-crustal rocks in the north (Mulga Park Subdomain) on the
83 moderately to shallowly south-dipping Woodroffe Thrust (Camacho et al., 1995; Major and Conor, 1993). The
84 intracontinental Petermann Orogeny correlates in time with the global Pan-African Orogeny (Camacho et al., 1997)
85 and was possibly caused by a clockwise rotation of the South and West Australian Cratons with respect to the North
86 Australian Craton (Li and Evans, 2011). The protoliths of the Fregon and Mulga Park Subdomains are very similar in
87 composition and age (Camacho and Fanning, 1995; Edgoose et al., 1999), but can be readily distinguished using
88 airborne thorium (Th) concentrations as seen in Figure 2c. The low Th concentration in the hanging wall is probably
89 related to formation and migration of partial melts to shallower crustal levels during granulite facies metamorphism,
90 with the breakdown of apatite and monazite resulting in partitioning of incompatible elements, such as Th, into the
91 melt phase (Förster and Harlov, 1999). Low Th concentrations can, therefore, be indicative of dry lower crustal rocks
92 (Lambert and Heier, 1968; Scharbert et al., 1976). The signal is partly obliterated by the granitic intrusions of the
93 Pitjantjatjara Supersuite and Giles Event, which succeeded granulite facies metamorphism.



94

Figure 2: a) Total magnetic intensity map (Geoscience Australia, 2015) and interpreted structures. Most fault zones appear as dark lines with a marked contrast, lithological layering is visible in the Mulga Park Domain (MPD) whereas the sediments of the Leveger Basin (LB) appear blurred. b) Interpretation of the tectonic framework of the Central Musgrave Block. The Mann Fault (MF) separates units that did not experience high grade overprint during the Petermann Orogeny (in blue south (blue), from the Fregon Domain (FD, purple) in the north. The Davenport Shear Zone (DSZ), North Davenport Shear Zone (NDSZ) and the Woodroffe Thrust (WT) were mapped by integrating the magnetic intensity map with airborne imagery and direct field observations. c) Compilation of airborne gamma ray surveys, with concentration of Thorium shown from blue (low) to red (high). Flares of low concentration in the footwall are associated with sediments transported from the hanging wall by rivers. Pseudotachylyte sample locations discussed in the text are indicated as black stars. Dataset SA_RAD_TH from PIRSA (2011), grey levels from hill shade.

95 3 Field observations

96 The Davenport Shear Zone (DSZ) is a strike-slip shear zone trending WNW-ESE with a sub-horizontal stretching
 97 lineation, a moderately steeply dipping foliation (Camacho et al., 1997), and a sense of shear that changes from
 98 dominantly sinistral to central from west to east. In the framework of the Musgrave Block, it is bounded to the south



99 by the generally poorly exposed Mann Fault (Fig. 2a). While dextral strike-slip movement along the Mann Fault is
100 indicated by the pull-apart Levenger Basin (Aitken and Betts, 2009; Camacho and McDougall, 2000), a normal, north-
101 side up component is implied by the lack of any known high-pressure Petermann Orogeny overprint south of the Mann
102 Fault (Glikson, 1996). To the north, deformation in the DSZ is strongly partitioned and bounded by a high-strain zone
103 localized on a series of dolerite dykes. The only continuous zone of mylonites north of the DSZ towards the Woodroffe
104 Thrust is the coeval North Davenport Shear Zone (Camacho et al., 1997). This mylonitic zone also localized on a
105 series of dolerite dykes and developed under similar conditions to the DSZ, but the pitch of the lineation is widely
106 variable, from horizontal to down dip to the south, with the shear sense being dominantly dextral oblique thrusting
107 towards NW. The DSZ mylonites and the NDSZ converge in the west. Towards the east, the relationships are less
108 clear because of the lack of outcrop. The ENE trending, moderately dipping Ferdinand Shear Zone is a sinistral strike-
109 slip shear zone that appears to branch from the steep Mann Fault (Conor, 1987).

110 The DSZ is an approximately 5 km wide mylonitic zone with the foliation trend clearly visible on satellite images.
111 This foliation encompasses domains of low strain, from kilometre to metre scale, which potentially preserve initial
112 stages of the temporal development of deformation. Pseudotachylytes are abundant, not only in the DSZ, but
113 throughout the whole Fregon Subdomain. They are concentrated along, but not exclusively limited to, the different
114 shear zones described above and especially along the Woodroffe Thrust (Camacho et al., 1995). Pseudotachylytes are
115 easily identified in the field by their fine-grained matrix, abundance of clasts, injection veins, breccias and chilled
116 margins (Fig. 3). When overprinted by subsequent ductile shearing, identification becomes more difficult and cannot
117 always be confirmed (Kirkpatrick and Rowe, 2013; Price et al., 2012). The thickness of pseudotachylyte veins reaches
118 up to 7 cm but is usually about 1 cm. Generation surfaces, when observed, show very little former melt, as it was
119 mostly injected into the host rock. There is no evidence for hydration, such as formation of bleached halos or hydrous
120 mineral growth. In all the different mylonitic shear zones of the Fregon Subdomain, the observed relative age
121 relationship between pseudotachylyte formation and ductile shearing in the adjacent rock covers the following range
122 of possibilities.

- 123 (1) Pseudotachylyte post-dates shearing. The mylonitic foliation in the host rock is crosscut and brecciated by
124 the pseudotachylytes (Fig. 3a), which often localized parallel to the foliation, in some cases at the boundary
125 to ultramylonite bands or along the rim of dolerite dykes (Fig. 3b). They appear as fine grained black veins
126 or as breccias with a black fine-grained matrix, in which fragments of the host rock show a rotated internal
127 fabric.
- 128 (2) Pseudotachylyte is broadly synchronous with shearing. Pseudotachylyte veins crosscut the mylonitic foliation
129 and are themselves foliated, as visible from elongated clasts (Fig. 3c). The stretching lineation in the
130 pseudotachylyte is parallel to that in the surrounding mylonites. Veins and breccias can show a wide range
131 of matrix colours, from grey to beige to caramel-coloured.



132 (3) Foliated pseudotachylyte occurs in effectively unsheared rocks, with ductile shearing concentrated
 133 exclusively within the pseudotachylyte vein, while the adjacent rock remained coarse grained and without
 134 discernible mylonitisation (Figs. 3d, 4).

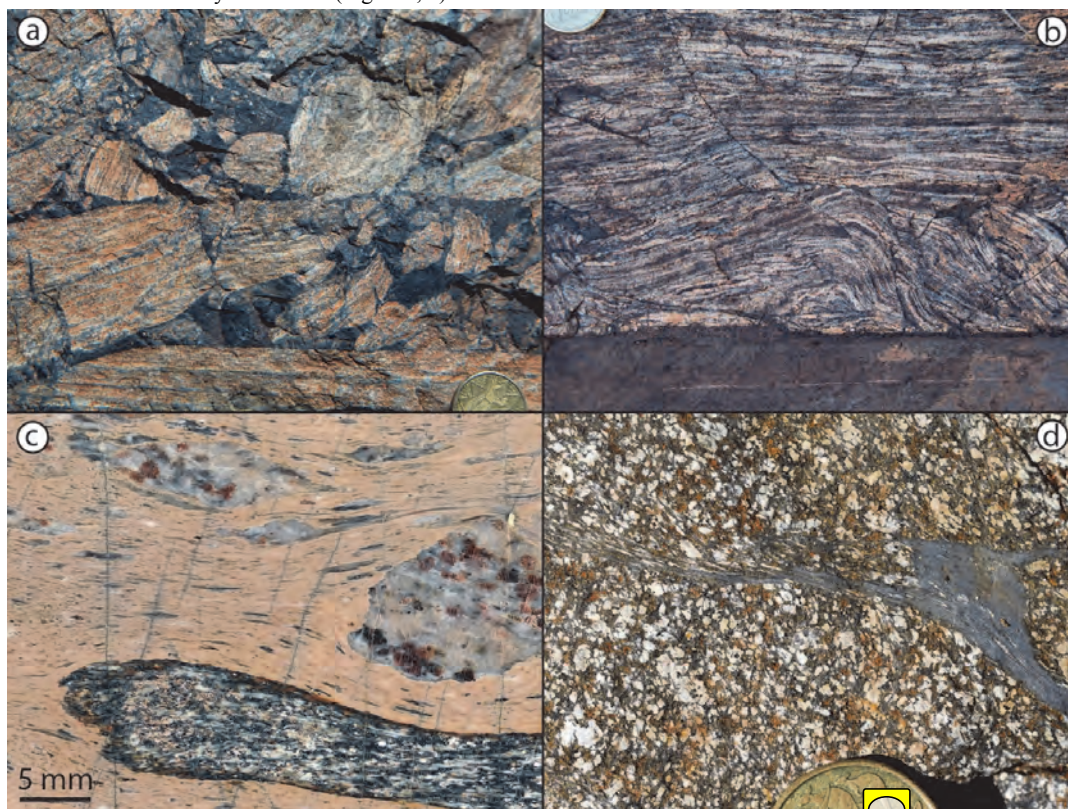
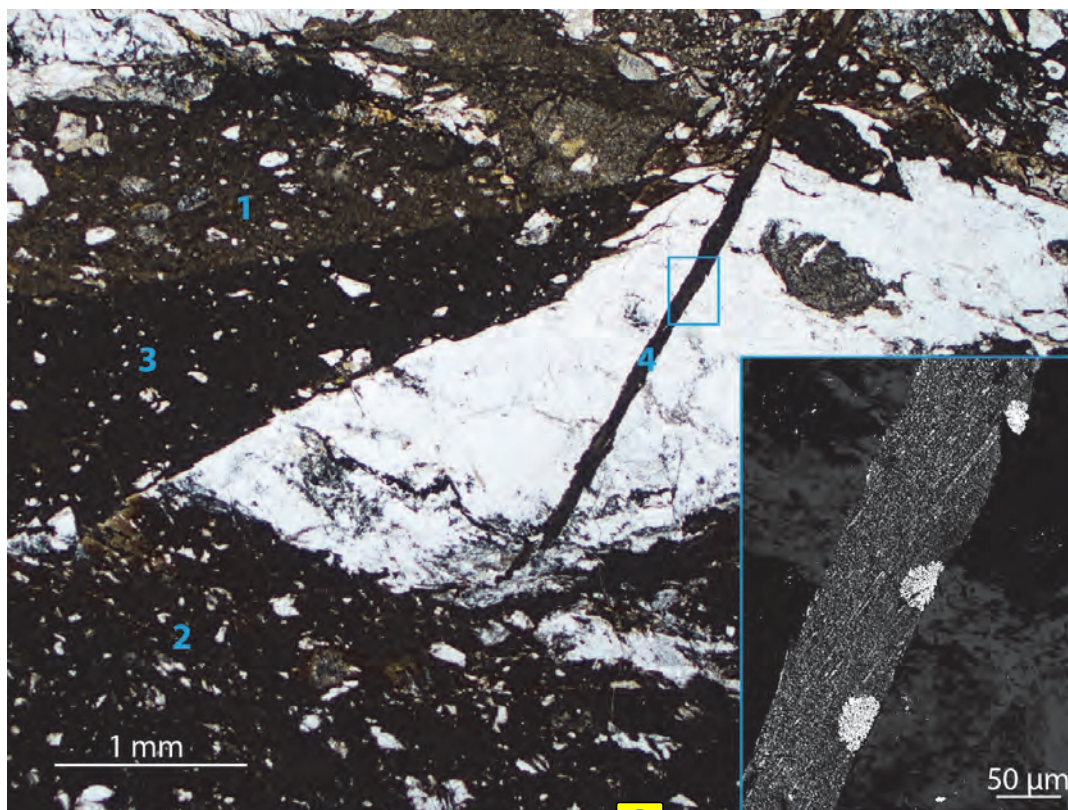


Figure 3: Field examples of pseudotachylytes: (a) Pseudotachylyte veins disrupting mylonitic foliation (26.3877 S, 131.7091 E). (b) Late stage pseudotachylyte localizing at the boundary of a sheared dolerite dyke, creating a duplex-like structure with all planes of movement decorated by pseudotachylytes (N is up, 26.3408 S, 131.5255 E). (c) Polished slab with caramel-coloured pseudotachylyte including fragments of quartzofeldspathic gneiss and of a mafic granulite. Note the internal foliation and elongation of clasts (26.3853 S, 131.7105 E). (d) Sheared pseudotachylyte in an otherwise undeformed gabbro (N is up, 26.3528 S, 131.8419 E).



135 Figure 4: Thin section image of sample F44 (26.4514 S, 131.9553 E) showing four generations of pseudotachyrites (plane polarized light; to reduce contrast, images taken with different exposure times were combined). Inset: backscattered electron image of the area indicated by the blue box: a vein of generation four, which shows a foliation oblique to the vein boundary and dendritic overgrowth on the matrix.

136 **4 Microstructure**

137 **4.1 Post-shearing pseudotachylyte**

138 Late-stage pseudotachylytes crosscut the mylonitic fabric, and show the pristine characteristic microstructures of
139 quenched melts, preserving an extremely fine-grained matrix (grain size on the order of a few microns) with flow
140 structures, chilled margins and angular, sometimes corroded, clasts (Fig. 5a). In some cases, microlites of feldspar and
141 pyroxene are observed. Since this paragenesis is the result of quenching, their mineral assemblages and mineral
142 chemistry do not represent ambient temperature conditions.



143 4.2 Syn-shearing pseudotachylyte

144 Sheared pseudotachylytes on occasion contain clasts of an older generation of pseudotachylyte, suggesting a cyclicity
145 of brittle and ductile deformation. The characteristic colour (Fig. 3c) in the field is a result of fine grained poikilitic garnet
146 (<20 µm, Fig. 5b). The syn-kinematic mineral assemblage of pseudotachylytes does not show any evidence for fluid
147 infiltration.

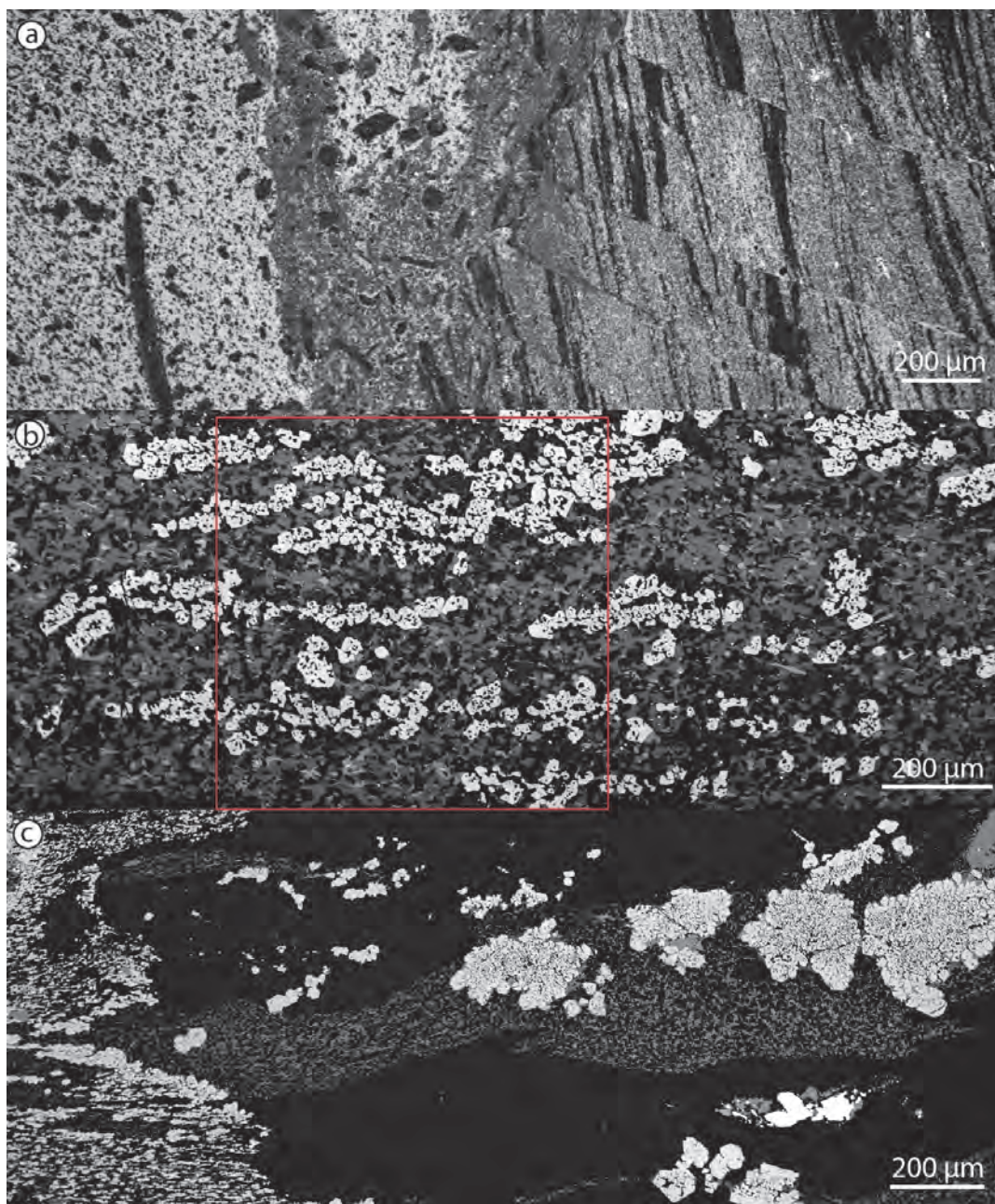
148 Sample F68 is a garnet-bearing quartzo-feldspathic gneiss, sampled close to the northern boundary of the DSZ (same
149 outcrop as the example in Figure 3c; 26.3849 S, 131.7067 E). Pseudotachylyte veins are ca. 1 mm thick, spaced ca. 1
150 cm apart, and oriented parallel to the protomylonitic foliation. Pseudotachylyte veins show injections and have a fine-
151 grained matrix of Grt+Kfs+Pl+Qz+Bt+Ky. Internal foliation is defined by biotite and aggregates of garnet (Fig.
152 5b). In the host rock, mm-sized remnant granulite facies garnets are fractured and surrounded by smaller,
153 neocrystallized garnet, with sizes on the order of tens of microns.

154 A sheared pseudotachylyte was sampled in the immediate hanging wall of the Woodroffe Thrust (S5, 26.3082 S,
155 131.7745 E), at the boundary between a sheared dolerite dyke and undeformed felsic granulite (sample S5). This
156 pseudotachylyte has a similar paragenesis as the dolerite dyke, but is much finer grained. The boundary with the
157 dolerite is decorated with even finer grained garnet, possibly the remnant of a chilled margin with a slightly different
158 composition. Where the pseudotachylyte injected into the granulite, it evaded shearing and shows a fine-grained matrix
159 with dendritic garnet overgrowth (Fig. 5c) and flow banding is occasionally preserved (Figure A1).

160 4.3 Sheared pseudotachylyte in undeformed host rock

161 Sample F44 from the Ferdinand Shear Zone (26.3856 S, 131.9550 E) hosts at least four generations of pseudotachylyte
162 veins and breccias in a granitic host rock (Fig. 4). Individual pseudotachylyte veins vary in the amount and rounding
163 of clasts, compositional heterogeneity, and recrystallized assemblage. The modal abundance of recrystallized minerals
164 Grt+Cpx+Opx+An+Fs (mineral abbreviations after Whitney and Evans, 2010) is also variable, possibly reflecting
165 a progressive change in bulk chemistry of the melt. Generations three and four clearly crosscut older generations and
166 are themselves sheared. The youngest generation (4) is further decorated with dendritic garnet along the margin of the
167 vein.

168 Sample F6 is a gabbro assigned to the Giles Complex (Fig. 3d, 26.3528 S, 131.8419 E), which largely preserves its
169 magmatic texture but contains sheared pseudotachylyte. The host rock is effectively unshaped and shows static
170 reactions such as Grt coronas around Pl in contact with Cpx and breakdown of Opx and Pl to Cpx. The pseudotachylyte
171 contains a large number of dominantly Pl- and Kfs-clasts (ca. 50% of the total volume), which show limited
172 recrystallization and reaction. The matrix of the recrystallized pseudotachylyte consists of
173 Grt+Cpx+Kfs+Qz+Mag+Rt+Ilm+Ky.



174

Figure 5: Backscattered electron images of pseudotachylyte: (a) Late-stage pseudotachylyte with angular clasts in mylonitic host rock with abundant fractures (26.3550 S, 131.8432 E). (b) Recrystallized and sheared pseudotachylyte in sample F68. Minerals in greyscale from dark to bright: Qz, Pl, Kfs, Ky, Bt, Grt. Red box indicates the mapped area for Figure 2-6. (c) Unsheared pseudotachylyte in a vein cutting through a feldspar grain of the granulitic host rock showing garnitic overgrowth of garnet. In the left part of the image, the pseudotachylyte is fine grained and foliated (sample S₂₇).



175 **5 Conditions of pseudotachylyte emplacement**

176 **5.1 Methods**

177 Backscattered electron images (BSE) were taken with a Quanta 200F, equipped with a field emission gun deployed at
178 the ScopeM (Scientific Center for Optical and Electron Microscopy, ETH Zurich). Quantitative measurements of
179 mineral composition were acquired with a JEOL JXA-8200 electron probe micro analyser (EPMA) at the Institute for
180 Geochemistry and Petrology, ETH Zurich, with a set of natural standards for analysis. Voltage was reduced from 15
181 kV to 10 kV for some samples to account for the fine grain size. Thermodynamic modelling using Perple_X (Connolly,
182 1990) was carried out on three samples of recrystallized pseudotachylytes within different host rocks. The
183 determination of a bulk composition for pseudotachylytes by using the classic XRF-method (X-Ray Fluorescence) is
184 hampered by their geometry and the presence of abundant clasts (Di Toro and Pennacchioni, 2004). To minimize these
185 problems, the Matlab toolbox XMapTools (Lanari et al., 2014) was used to calculate the bulk composition from WDS-
186 maps (wavelength dispersive spectrometer) collected with the EPMA. Quantitative point analysis was used to
187 “standardize” the maps (Lanari et al., 2014). Here, the weight per cent of a point analysis is linked to counts for each
188 element of the same point on the map. This can be done for each mineral phase separately to account for matrix effects.
189 After correlating the counts to weight per cent of all pixels, the bulk composition of the pseudotachylyte for the desired
190 area of the map can be extracted and used as input for Perple_X. For all samples, a standardization for each separate
191 mineral was impossible because of the fine grain size. Instead, all count values on the map were correlated to a mean
192 weight per cent value from point analysis. The resulting deviation in mineral chemistry is generally low and was
193 corrected manually by comparing exported compositions from the standardized maps with measured analyses. The
194 bias on the bulk composition induced by the choice of area can be tested by using a Monte Carlo approach (integrated
195 in XMapTools). The deviations in weight per cent (wt%) are in the order of 0.4 for silica and much lower for the other
196 elements. The thermodynamic dataset of (Holland and Powell, 1998) was used to calculate pseudo-sections for the
197 composition of the samples and a range of P-T-conditions to compare with the observed assemblage in recrystallized
198 pseudotachylyte. The solution models used can be found in the appendix (Table B1-3).

199 **5.2 Results**

200 **5.2.1 Syn-shearing pseudotachylyte**

201 The pseudotachylyte veins in sample F68 have a rather homogeneous phase distribution with a relatively large grain
202 size, and are almost devoid of clasts (Fig. 5b). The compositional (WDS) map has a size of 400x400 pixels and
203 measurements were made using a step size of 2 μm , resulting in an area of 0.64 mm^2 . The amount of water in the rock



204 could not be measured directly, and was calculated using the
 205 3 wt% water in biotite and its modal abundance, since biotite
 206 is the only water-bearing mineral. As biotite is a platy
 207 mineral, its area in the section parallel to the lineation and
 208 perpendicular to the foliation might be under-represented.
 209 However, an arbitrary threefold increase of bulk water
 210 content in the calculations (from 0.05 to 0.15 wt%) does not
 211 have a noticeable effect on the stability fields of the mineral
 212 phases. The stability field for the assemblage of the
 213 recrystallized pseudotachylyte in sample F68 is rather wide
 214 and pressure-temperature conditions can be further
 215 delimited with mineral isopleths (Fig. 6). The conditions
 216 estimated are around 1.05 GPa and 600 °C. The
 217 stoichiometry for each mineral can be reproduced relatively
 218 reliably (Table B1).

219 In sample S5, the pseudotachylyte shows strong
 220 compositional heterogeneity parallel to the foliation,
 221 probably due to differences associated with original flow banding. This is best visible in the Ca-compositional map of
 222 Figure 7a, where areas 1 and 2 show lower Ca-content in plagioclase with respect to the other areas. Areas 1, 2 and 3
 223 have a similar paragenesis of Grt+Cpx+Pl+Kfs+Rt, with Qz limited to area 2, while area 3 also lacks Kfs. Areas 4 and
 224 5 consist of Grt+Cpx+Pl+Bt+Opx+Rt. A bulk composition was calculated individually for each area. Clasts of Ca-
 225 rich Pl are present (see upper right corner of 7a for an example), with Ky needles growing inside the clasts but not in
 226 the matrix assemblage. These Pl-clasts were masked out for the calculation of the local bulk composition since they
 227 are not part of the stable assemblage. Calculated pseudosections for each area were superimposed onto each other to
 228 narrow down the P-T estimates of coeval formation (Fig. 7b). Area 4 was not considered, since modelling predicted
 229 sapphirine to be stable, which was not observed in the sample. Otherwise, the stable assemblage field for area 4
 230 overlaps largely with those of the other areas. The stability of Cpx with the bulk compositions of areas 4 and 5 is
 231 limited to a maximum pressure of about 0.8 GPa. Since Opx occurs as coronas around Cpx, we assume that Opx-
 232 growth is post kinematic (see area 5 in Fig. 7a, where Opx appears as small dark blue dots around the Cpx). Opx was
 233 therefore not considered to be stable in the sheared paragenesis of area 5. The pseudosections show an overlap of the
 234 different stable parageneses for their respective local bulk composition (Fig. 7b). The shared stability field spans the
 235 range 1.1-1.3 GPa and 670-710 °C. The compositions of individual phases derived from the Perple_X model,
 236 calculated at 1.2 GPa and 690 °C, are in good agreement with the measured compositions (Table B2).

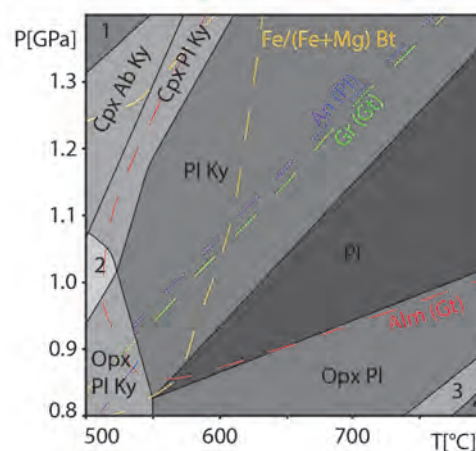
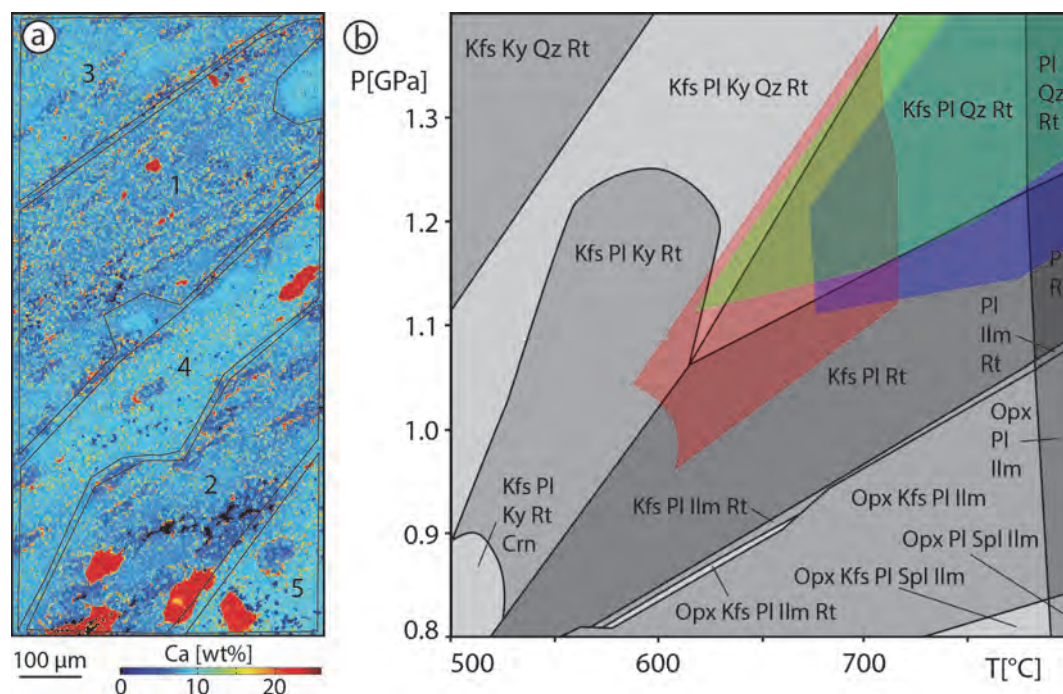


Figure 6: Pseudosection calculated for F68. Additional phases in all fields: Kfs+Grt+Bt+Qz+Rt. With isopleths for Fe/(Fe+Mg) in biotite, anorthite component of plagioclase (An (Pl)), grossular and almandine component of garnet (Gr, Alm (Gt)). Numbered Fields: 1: Cpx, Ky; 2: Opx, Cpx, Pl, Ky; 3: Opx, Pl, Ilm; 4: Opx, Pl, Ilm, no Rt



237

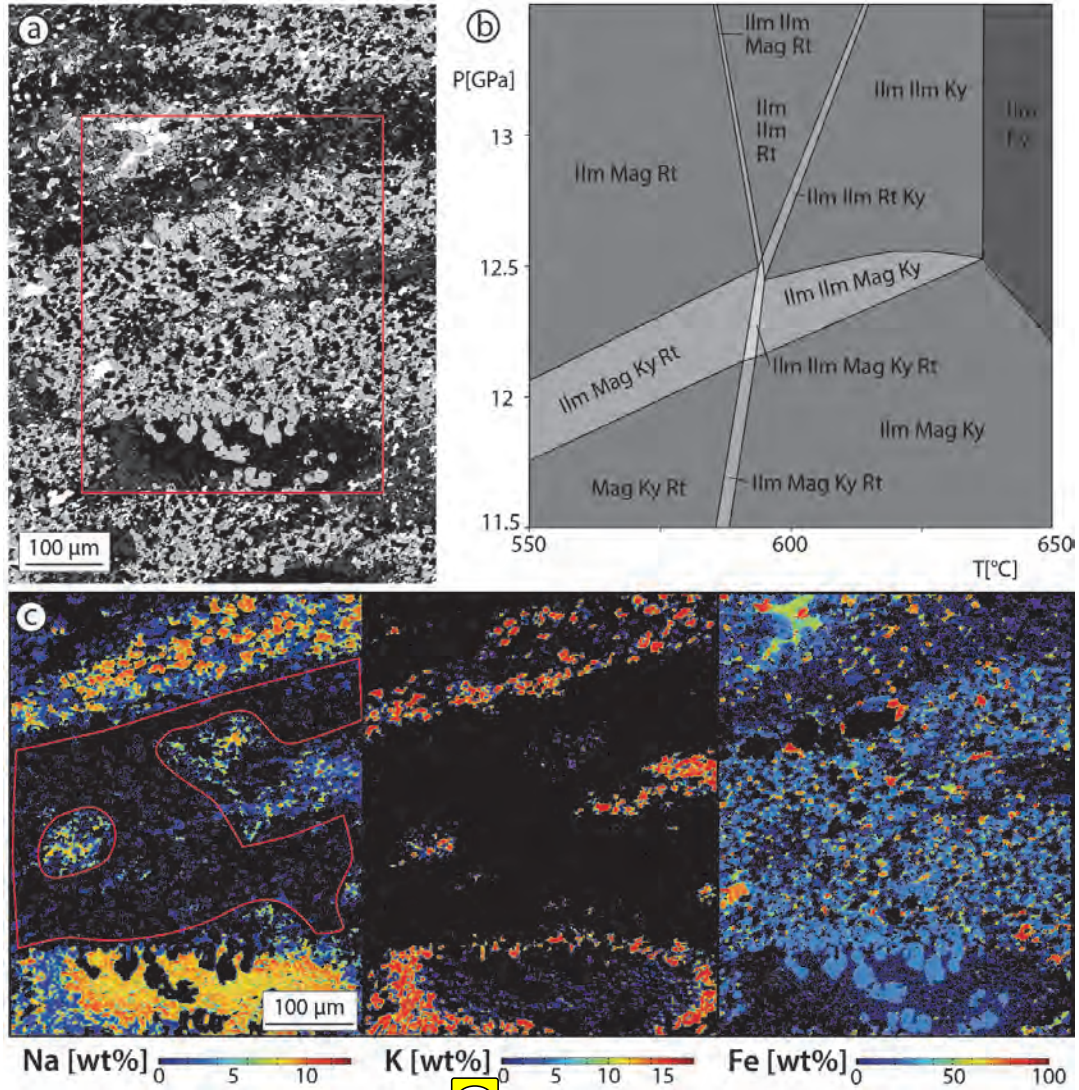
Figure 7: Quantified X-ray map for Ca for sample S5 with a step size of 2 μm and 250x500 pixels. Minerals visible: red: Cpx, dark blue: Grt, medium blue: low-Ca Pl, light blue: high-Ca Pl. Areas are defined by the Pl-composition. b) Pseudosection for sample S5, area 2, all parageneses also have Grt+Cpx. Overlays of the observed stability fields for parageneses from pseudosections from the other areas: red: area 1, green: area 3, blue: area 5. For the microstructural context of the area, see Figure A2.

238 5.2.2 Sheared pseudotachylyte in undeformed host rock

239 The pseudotachylyte in the gabbroic sample (F6) is extremely fine grained and is dominated by millimetre-sized clasts
 240 of plagioclase, which only partly reacted to form garnet and K-feldspar. The compositional (EDS) map was collected
 241 with a step size of 1 μm and 400x500 pixels, to account for the small grain size. The area is located between a remnant
 242 Pl-clast, overgrown by Grt with the rim replaced by Kfs, and a ribbon of mixed Kfs and Pl (Figs. 8a,c). The area in
 243 between, with abundant Grt+Apt+Mag, is interpreted to have directly recrystallized from the former pseudotachylyte
 244 melt during shearing. Smaller Fsp-clasts were masked out during determination of the local bulk composition because
 245 reactions and mixing seem to be incomplete. Apatite was removed completely for the calculation of the composition.
 246 Because of the high content of Fe³⁺-bearing minerals such as ilmenite and magnetite (Fig. 8c), Fe²⁺/Fe³⁺ was calculated
 247 using the volume per cent of each iron bearing phase and their respective Fe²⁺/Fe³⁺. The calculated pseudosection
 248 (Fig. 8b) shows a narrow area for the observed assemblage of Grt+Cpx+Kfs+Qz+Ilm+Rt+Mag+Ky at conditions of
 249 1.23 GPa and 590 °C. Rutile only appears as exsolution from the Ti-rich ilmenite, which is a reaction taking place
 250 close to these conditions. Initial calculations were done with the clinopyroxene solution model used for the other
 251 samples, resulting in lower pressures (ca. 1.15 GPa), but predicted much higher Na-content in the Cpx of 6.5 wt%



252 compared to the measured 2 wt%. The Cpx-model used for the final calculations yields compositions much closer to
 253 those measured (Table B3).



254

Figure 8: a) BSE image of a sheared pseudotachylyte with partly recrystallized clasts. Red box indicates the location of the X-ray-map. b) Results from thermodynamic modelling using Perple_X with an estimate for the conditions of shearing at about 1.23 GPa and 590 °C. Minerals stable in all fields: Grt, Cpx, Kfs, Qz. c) Compilation of X-ray maps: Na-map shows the incomplete breakdown of a Pl-clasts in the bottom of the image and the replacement with Kfs (K-map). Red outline shows the extracted area of the bulk composition used. Fe-map shows abundant Mag (red) and two distinct Ilm populations (orange and yellow).



255 6 Summary

256 Multiple crosscutting sheared pseudotachylytes can be interpreted as a cyclic interplay of brittle and ductile
257 deformation. Hence the pressure and temperature conditions derived from the recrystallized assemblage of sheared
258 pseudotachylyte are interpreted to be close to the ambient host rock conditions of pseudotachylyte formation and
259 injection. Results from thermodynamic modelling are around 1.0-1.3 GPa and 600-700 °C. These results are very
260 similar to the estimated conditions of mylonitisation in the Fregon Domain during the Petermann Orogeny of 650 °C
261 and 1.2 GPa (Camacho et al., 1997).

262 Lin (2008) described pseudotachylytes in the hanging wall of the Woodroffe Thrust and interpreted them to have been
263 generated during Musgravian granulite facies metamorphism. This interpretation can be ruled out for two main
264 reasons: 1) The hanging wall of the Woodroffe Thrust experienced granulite facies metamorphism during the c.a. 1.2
265 Ga Musgravian Orogeny but all pseudotachylytes observed in the field and described in Lin (2008) are associated
266 with structures related to the ca. 550 Ma Petermann Orogeny. 2) Pseudotachylytes are present in gabbros (Fig. 3d)
267 and dolerite dykes (Fig. 3b) that intruded during the ca. 1.07 Ga Giles Event and dolerite dykes of the ca. 800 Ma
268 Amata Suite. All these magmatic rocks were intruded well after the granulite facies metamorphism associated with
269 the Musgravian Orogeny.

270 7 Discuss



271 Pseudotachylyte development by brittle failure and frictional seismic slip (McKenzie and Brune, 1972; Sibson, 1975)
272 is the favoured mechanism to explain the field observations in the Fregon Domain. Alternative processes involving
273 thermal runaway during ductile shear (John et al., 2009; Thielmann et al., 2015) or ductile instabilities (Hobbs et al.,
274 1986) require that a pseudotachylyte-bearing fault necessarily had a ductile precursor. This is not in accord with the
275 observation that many pseudotachylytes occur in otherwise unsheared host rocks and act as a precursor for subsequent
276 ductile shearing, rather than the other way around. In addition, pseudotachylytes within undeformed host rock do not
277 necessarily contain clasts of mylonites.

278 Brittle deformation under elevated temperatures at depths below the classic brittle-ductile transition zone in felsic
279 continental crust might be explained by local high fluid pressure promoting fracturing (Altenberger et al., 2011; Lund
280 and Austrheim, 2003; Steltenpohl et al., 2006; White, 2012), either due to dehydration reactions or fluid infiltration.
281 However, these mechanisms can be excluded for the examples presented here, because most host rocks (in particular
282 the felsic granulites) were already thoroughly dehydrated during the earlier granulite facies Musgravian Orogeny and
283 there is no evidence of fluid infiltration during the Petermann Orogeny. As seen for example in sample S5, the hydrous
284 mineral biotite is restricted to isolated domains indicating that the activity of OH was low. The absence of hydration
285 associated with pseudotachylyte development in the Fregon shear zones also indicates that, in contrast to what is
286 observed in the Bergen Arc (Norway), the switch between brittle (pseudotachylyte) and ductile shearing was not
287 induced by infiltration of fluids, promoted by the propagation of the earthquake fracture, and by the associated
288 weakening due to metamorphic reaction (Austrheim, 2013, and references therein). In the absence of elevated pore
289 fluid pressure, high stresses are necessary to fracture rocks under dry, lower crustal conditions (Sibson and Toy, 2006).



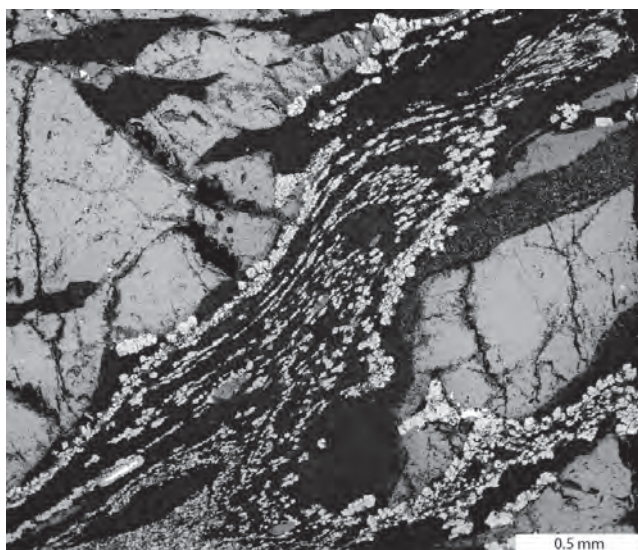
290 Natural examples of shear zones with small grain sizes developed under amphibolite facies conditions suggest that
291 mid- and lower crust can be strong (Fitz Gerald et al., 2006; Menegon et al., 2011). This might explain initial
292 fracturing, but on the long term, shear zones show localization of strain and therefore indicate weakening of the rocks.
293 To explain the observed cyclicity of fracture and flow, temporal stress variations are necessary. Transient high stresses
294 in the mid- to lower crust have been proposed to result from a downward propagation of stresses from the usual
295 seismogenic zone (<15 km) during seismic failure (Ellis and Stöckhert, 2004a; Moecher and Steltenpohl, 2009). In
296 the example of the 2015 Gorkha earthquake on the Main Himalayan Thrust (Duputel et al., 2016), there are indeed
297 aftershocks located in the deeper crust following an earthquake at about 15 km depth. While it is hard to test this
298 model from field observations, the implication of this concept based on downward migration of seismicity is that for
299 each event recorded in the lower crust (> 30 km depth), such as the pseudotachylytes in the Davenport Shear Zone,
300 there was necessarily a large earthquake with a source in the upper crust (< 15 km). However, this is not observed for
301 many large, lower crustal earthquakes, for example in the Indian Shield (Mitra et al., 2004). Considering the abundance
302 of pseudotachylytes in the lower crustal Fregon Domain, this would imply a correspondingly large and perhaps
303 unrealistic amount of strong seismicity in the upper crust, suggesting that such localized pseudotachylytes may have
304 had a local trigger in the dry lower continental crust.

305 **8 Conclusions**

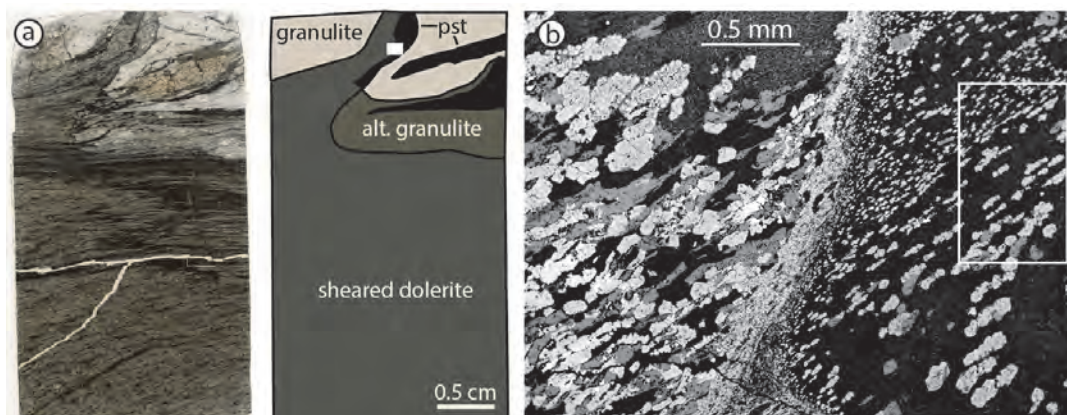
306 The Fregon Domain documents seismic fracturing under lower crustal conditions of around 1.0-1.3 GPa and 600-700
307 °C in an intracontinental setting. Repeated episodes of brittle failure and ductile creep represent recurring earthquake
308 cycles and a strong variation of stress in a water deficient lower crust. It is questionable whether current models of
309 downward propagation of seismic stresses from the “seismogenic” upper crust can explain the observed repeated
310 cyclic brittle failure and ductile shearing sporadically distributed over such a wide area. It seems more likely that these
311 earthquake cycles are locally triggered in the dry lower continental crust, at least in this intracontinental setting.
312 Models should therefore take into account temporal and spatial variations of stress in a heterogeneously deforming
313 lower crust.



314 **Appendix A, additional images**



315 **Figure A1: BSE-image of injection vein, original flow banding is visible by the selective garnet overgrowth on some layers.**



316 **Figure A2: Microstructural context of area mapped in sample S5 (Fig. 7): a) Plane polarized light microscopic image and**
317 **sketch of the thin section, with box indicating image in b). b) BSE image of the boundary between dolerite (left) and sheared**
318 **pseudotachylyte, with the white box indicating area in Figure 7a.**

319 **Appendix B, Bulk and mineral chemistry**

	Bulk	Grt_m	Grt_c	Pl_m	Pl_c	Kfs	Kfs_c	Ky_m	Ky_c	Bt_m	Bt_c
Na ₂ O	1.06	0.02	0.00	8.77	8.14	0.89	1.33	0.00	0.00	0.19	0.00
MgO	2.67	8.31	9.28	0.01	0.00	0.00	0.00	0.00	0.00	19.04	18.56
Al ₂ O ₃	12.76	22.61	22.30	21.93	24.20	18.92	18.56	62.40	62.92	14.73	17.67
SiO ₂	70.2	38.55	39.42	58.69	61.49	63.10	65.08	36.66	37.08	37.61	37.61
K ₂ O	3.77	0.02	0.00	0.19	0.55	15.53	14.91	0.00	0.00	10.19	10.76
CaO	1.98	5.83	5.63	5.40	5.61	0.05	0.12	0.03	0.00	0.01	0.00
TiO ₂	0.79	0.08	0.00	0.04	0.00	0.01	0.00	0.04	0.00	3.97	4.75
MnO	0.23	0.92	0.88	0.01	0.00	0.00	0.00	0.05	0.00	0.00	0.01
FeO	5.85	23.72	22.48	0.11	0.00	0.19	0.00	1.12	0.00	7.36	7.60
H ₂ O	0.05*									3**	3.04
total	99.31	100.06	100.00	95.15	99.99	98.69	100.00	100.29	100.00	96.10	100.00
Cations											
Al		2.04	2.00	1.21	1.26	1.04	1.01	1.99	2.00	1.29	1.48
Si		2.96	3.00	2.75	2.73	2.94	2.99	0.99	1.00	2.79	2.68
		5.00	5.00	3.96	3.99	3.98	4.00	2.98	3.00	4.08	4.16
Fe		1.52	1.43							0.46	0.45
Mg		0.95	1.05							2.11	1.97
Mn		0.06	0.06								
Ca		0.48	0.46	0.27	0.27	0.00	0.01				
Na				0.80	0.70	0.08	0.12				
K				0.01	0.03	0.92	0.87			0.96	0.98
total		3.01	3.00	1.07	1.00	1.00	1.00			3.53	3.40

320 **Table B1: A3 Representative analysis for sample F68. m=measured; c=calculated from perplex at 1.2 GPa and 690 °C;**
 321 ***calculated: volume per cent Bt and 3 weight per cent water in Bt; **assumed; Solution models: Omph(GHP), GITrTsPg,**
 322 **melt(HP), Chl(HP), Sp(HP), Gt(GCT), Opx(HP), Mica(CHA1), Ctd(HP), St(HP), Bio(TCC), hCrd, Osm(HP), Carp(HP),**
 323 **Sud, feldspar, IlGkPy, Neph(FB), Chum**



	Area 1	Area 2	Area 3	Area 4	Area 5	Grt_m	Grt_c	Pl_m	Pl_c	Kfs_m	Kfs_c	Cpx_m	Cpx_c
Na ₂ O	4.42	3.89	5.59	5.60	4.72	0.00	0.00	6.71	6.97	0.19	1.47	1.23	1.47
MgO	4.79	5.37	2.56	2.44	4.16	11.52	11.25	0.06	0.00	0.09	0.00	15.71	15.05
Al ₂ O ₃	21.00	21.15	23.50	23.87	22.33	23.41	22.71	25.97	25.62	19.01	18.72	3.76	2.42
SiO ₂	52.30	52.04	54.99	55.45	53.85	40.16	40.14	59.33	59.30	64.04	64.94	51.85	55.20
K ₂ O	0.58	0.71	0.42	0.47	0.49	0.01	0.00	0.28	0.82	14.29	14.58	0.01	0.00
CaO	8.76	9.02	8.76	9.58	10.12	7.26	7.26	7.44	7.30	0.17	0.29	22.25	23.10
TiO ₂	0.41	0.36	0.38	0.35	0.33	0.03	0.00	0.10	0.00	0.04	0.00	0.20	0.00
MnO	0.15	0.16	0.12	0.11	0.12	0.35	0.52	0.01	0.00	0.00	0.00	0.02	0.00
FeO	5.12	5.92	2.30	1.13	2.47	18.17	18.12	0.13	0.00	0.45	0.00	3.75	2.78
H ₂ O	0.00	0.00	0.00	0.00	0.00								
total	97.53	98.62	98.62	99.00	98.58	100.91	100.00	100.02	100.00	98.28	100.00	98.78	100.00

324

Cations

Al	2.04	2.00	1.36	1.35	1.04	1.01	0.16	0.10
Si	2.97	3.00	2.64	2.65	2.98	2.99	1.92	2.00
	5.01	5.00	4.01	4.00	4.03	4.00		
Fe	1.12	1.13					0.12	0.08
Mg	1.27	1.25					0.87	0.81
Mn	0.02	0.03					0.00	0
Ca	0.58	0.58	0.36	0.35	0.01	0.01	0.88	0.90
Na			0.58	0.60	0.02	0.13	0.09	0.10
K			0.02	0.05	0.85	0.85	0.00	0.00
total	2.99	3.00	0.95	1.00	0.87	1.00	1.95	1.90

325 Table B2: Representative analysis for sample S5. m=measured; c=calculated from perplex at 1.2 GPa and 690 °C, all
 326 mineral chemistry from area 2; Solution models: Omph(GHP), GlTrTsPg, melt(HP), Chl(HP), Sp(HP), Gt(GCT), Opx(HP),
 327 Mica(CHAl), Ctd(HP), St(HP), Bio(TCC), hCrd, Osm(HP), Carp(HP), Sud, feldspar, IlGkPy, Neph(FB), Chum



	Bulk	Gt_m	Gt_c	Kfs_m	Kfs_c	Cpx_m	Cpx_c
Na ₂ O	0.17	0.01	0.00	0.67	0.10	1.99	2.35
MgO	3.76	6.27	5.90	0.04	0.00	11.96	10.18
Al ₂ O ₃	11.75	21.88	21.31	19.54	18.36	4.02	6.76
SiO ₂	53.22	38.79	38.54	62.81	64.75	52.46	49.90
K ₂ O	0.04	0.00	0.00	15.97	16.75	0.03	0.00
CaO	5.09	6.64	7.35	0.08	0.04	20.15	20.88
TiO ₂	3.24	0.10	0.00	0.04	0.00	0.25	0.00
MnO	0.38	0.92	0.82	0.01	0.00	0.09	0.00
FeO	14.90	26.43	25.37	0.69	0.00	9.07	3.84
Fe ₂ O ₃	7.87		0.77				6.08
H ₂ O	0.00						
total	100.41	101.04	100.05	99.84	100.00	100.01	99.99
Cations							
Al		1.99	1.96	1.07	1.00	0.18	0.30
Si		2.99	3.00	2.93	3.00	1.95	1.87
		4.98	4.96	4.00	4.00		
Fe		1.70	1.70			0.28	0.31
Mg		0.72	0.69			0.66	0.57
Mn		0.06	0.05				
Ca		0.55	0.61	0.00	0.00	0.80	0.84
Na				0.06	0.01	0.14	0.17
K				0.95	0.99		
total		3.03	3.05	1.01	1.00	1.89	1.89

328 Table B3: Representative analysis for sample F6. m=measured; c=calculated from perplex at 1.17 GPa and 590 °C; Fe₂O₃
 329 calculated on the basis of volume per cent of phases; Solution models Gt(WPH), IlHm(A), MtUl(A), Omph(HP), GlTrTsPg,
 330 melt(HP), Chl(HP), Sp(HP), Opx(HP), Mica(CHA1), Ctd(HP), St(HP), Bio(TCC), hCrd Sapp(HP), Osm(HP), Carp(HP),
 331 Sud, feldspar, Neph(FB)



332 **Author contribution**

333 All authors listed took part in at least two of the three field seasons, which formed the basis of this study. AC's previous
334 knowledge of the field area and the local people was essential for the success of the campaign. SW contributed to the
335 microprobe work. NM and GP developed the initial idea of the study and the project was financed by a Swiss National
336 Science Foundation (SNF) Grant awarded to NM. FH prepared the manuscript with contributions from all co-authors.


337 **Acknowledgements**

338 We gratefully acknowledge permission granted to work on the Anangu Pitjantjatjara Yankunytjatjara Lands (APY) to
339 carry out our field work in the area. The Northern Territory Geological Survey (NTGS) and Basil Tikoff (Department
340 of Geoscience, University of Wisconsin) are thanked for their logistical support and the Nicolle family of Mulga Park
341 station for their hospitality. The Scientific Center for Optical and Electron Microscopy (ScopeM) provided the
342 facilities for the SEM work, and help by Karsten Kunze is especially acknowledged. The EMPA work was supported
343 by Eric Reusser and Lukas Martin. This project was financed by the Swiss National Science Foundation (SNF) Grant
344 200021_146745.

345 **References**

- 346 Aitken, A. R. A. and Betts, P. G.: Multi-scale integrated structural and aeromagnetic analysis to guide tectonic models:
347 An example from the eastern Musgrave Province, Central Australia, *Tectonophysics*, 476(3–4), 418–435,
348 doi:10.1016/j.tecto.2009.07.007, 2009.
- 349 Aitken, A. R. A., Smithies, R. H., Dentith, M. C., Joly, A., Evans, S. and Howard, H. M.: Magmatism-dominated
350 intracontinental rifting in the Mesoproterozoic: The Ngaanyatjarra Rift, central Australia, *Gondwana Res.*, 24(3–4),
351 886–901, doi:10.1016/j.gr.2012.10.003, 2013.
- 352 Austrheim, H. and Andersen, T. B.: Pseudotachylytes from Corsica: fossil earthquakes from a subduction complex,
353 *Terra Nova*, 16(4), 193–197, doi:10.1111/j.1365-3121.2004.00551.x, 2004.
- 354 Austrheim, H. and Boundy, T. M.: Pseudotachylytes Generated During Seismic Faulting and Eclogitization of the
355 Deep Crust, *Science*, 265(5168), 82–83, doi:10.1126/science.265.5168.82, 1994.
- 356 Austrheim, H., Erambert, M. and Boundy, T. M.: Garnets recording deep crustal earthquakes, *Earth Planet. Sci. Lett.*,
357 139(1–2), 223–238, doi:10.1016/0012-821X(95)00232-2, 1996.
- 358 Camacho, A. and Fanning, C. M.: Some isotopic constraints on the evolution of the granulite and upper amphibolite
359 facies terranes in the eastern Musgrave Block, central Australia, *Precambrian Res.*, 71(1), 155–181, 1995.
- 360 Camacho, A. and McDougall, I.: Intracratonic, strike-slip partitioned transpression and the formation and exhumation
361 of eclogite facies rocks: An example from the Musgrave Block, central Australia, *Tectonics*, 19(5), 978–996, 2000.
- 362 Camacho, A., Vernon, R. H. and Fitz Gerald, J. D.: Large volumes of anhydrous pseudotachylyte in the Woodroffe
363 Thrust, eastern Musgrave Ranges, Australia, *J. Struct. Geol.*, 17(3), 371–383, 1995.
- 364 Camacho, A., Compston, W., McCulloch, M. and McDougall, I.: Timing and exhumation of eclogite facies shear
365 zones, Musgrave Block, central Australia, *J. Metamorph. Geol.*, 15, 735–751, 1997.
- 366 Connolly, J. A. D.: Multivariable phase diagrams; an algorithm based on generalized thermodynamics, *Am. J. Sci.*,
367 290(6), 666–718, doi:10.2475/ajs.290.6.666, 1990.
- 368 Deichmann, N. and Rybach, L.: Earthquakes and temperatures in the lower crust below the northern Alpine foreland
369 of Switzerland, *Prop. Process. Earths Low. Crust*, 197–213, 1989.
- 370 Di Toro, G. and Pennacchioni, G.: Superheated friction-induced melts in zoned pseudotachylytes within the Adamello
371 tonalites (Italian Southern Alps), *J. Struct. Geol.*, 26(10), 1783–1801, doi:10.1016/j.jsg.2004.03.001, 2004.
- 372 Duputel, Z., Vergne, J., Rivera, L., Wittlinger, G., Farra, V. and Hetényi, G.: The 2015 Gorkha earthquake: A large
373 event illuminating the Main Himalayan Thrust fault: PROBING THE HIMALAYAN MEGATHRUST, *Geophys.*
374 *Res. Lett.*, 43(6), 2517–2525, doi:10.1002/2016GL068083, 2016.
- 375 Ellis, S. and Stöckhert, B.: Elevated stresses and creep rates beneath the brittle-ductile transition caused by seismic
376 faulting in the upper crust, *J. Geophys. Res.*, 109(B5), doi:10.1029/2003JB002744, 2004.
- 377 Evins, P. M., Smithies, R. H., Howard, H. M., Kirkland, C. L., Wingate, M. T. D. and Bodorkos, S.: Redefining the
378 Giles Event within the setting of the 1120–1020 Ma Ngaanyatjarra Rift, West Musgrave Province, Central Australia,
379 Geological Society of Western Australia, East Perth, W.A., 2010.
- 380 Fitz Gerald, J. D., Mancktelow, N. S., Pennacchioni, G. and Kunze, K.: Ultrafine-grained quartz mylonites from high-
381 grade shear zones: Evidence for strong dry middle to lower crust, *Geology*, 34(5), 369, doi:10.1130/G22099.1, 2006.



- 382 Förster, H.-J. and Harlov, D. E.: Monazite-(Ce)–huttonite solid solutions in granulite-facies metabasites from the
383 Ivrea-Verbano Zone, Italy, *Mineral. Mag.*, 63(4), 587–587, 1999.
- 384 Glikson, A. Y. and Australian Geological Survey Organisation, Eds.: *Geology of the western Musgrave Block, central*
385 *Australia, with particular reference to the mafic-ultramafic Giles Complex*, Australian Govt. Pub. Service, Canberra,
386 1996.
- 387 Goetze, C. and Evans, B.: Stress and temperature in the bending lithosphere as constrained by experimental rock
388 mechanics, *Geophys. J. Int.*, 59(3), 463–478, 1979.
- 389 Gray, C. M.: Geochronology of granulite-facies gneisses in the western Musgrave Block, Central Australia, *J. Geol.*
390 *Soc. Aust.*, 25(7–8), 403–414, doi:10.1080/00167617808729050, 1978.
- 391  Hobbs, B. E., Ord, A. and Teyssier, C.: Earthquakes in the Ductile Regime?, *PAGEOPH*, 124(1), 309–336, 1986.
- 392 Holland, T. J. B. and Powell, R.: An internally consistent thermodynamic data set for phases of petrological interest,
393 *J. Metamorph. Geol.*, 16(3), 309–343, 1998.
- 394 Jackson, J.: Faulting, flow, and the strength of the continental lithosphere, *Int. Geol. Rev.*, 44(1), 39–61, 2002.
- 395 Jackson, J. A., Austrheim, H., McKenzie, D. and Priestley, K.: Metastability, mechanical strength, and the support of
396 mountain belts, *Geology*, 32(7), 625–628, 2004.
- 397 John, T., Medvedev, S., Rüpke, L. H., Andersen, T. B., Podladchikov, Y. Y. and Austrheim, H.: Generation of
398 intermediate-depth earthquakes by self-localizing thermal runaway, *Nat. Geosci.*, 2(2), 137–140,
399 doi:10.1038/ngeo419, 2009.
- 400 Kirkpatrick, J. D. and Rowe, C. D.: Disappearing ink: How pseudotachylytes are lost from the rock record, *J. Struct.*
401 *Geol.*, 52, 183–198, doi:10.1016/j.jsg.2013.03.003, 2013.
- 402 Kohlstedt, D. L., Evans, B. and Mackwell, S. J.: Strength of the lithosphere: Constraints imposed by laboratory
403 experiments, *J. Geophys. Res. Solid Earth*, 100(B9), 17587–17602, doi:10.1029/95JB01460, 1995.
- 404 Lambert, I. B. and Heier, K. S.: Geochemical investigations of deep-seated rocks in the Australian shield, *Lithos*, 1(1),
405 30–53, doi:10.1016/S0024-4937(68)80033-7, 1968.
- 406 Lanari, P., Vidal, O., De Andrade, V., Dubacq, B., Lewin, E., Grosch, E. G. and Schwartz, S.: XMapTools: A
407 MATLAB©-based program for electron microprobe X-ray image processing and geothermobarometry, *Comput.*
408 *Geosci.*, 62, 227–240, doi:10.1016/j.cageo.2013.08.010, 2014.
- 409 Li, Z.-X. and Evans, D. A.: Late Neoproterozoic 40 intraplate rotation within Australia allows for a tighter-fitting and
410 longer-lasting Rodinia, *Geology*, 39(1), 39–42, 2011.
- 411 Lin, A.: Seismic Slip in the Lower Crust Inferred from Granulite-related Pseudotachylyte in the Woodroffe Thrust,
412 Central Australia, *Pure Appl. Geophys.*, 165(2), 215–233, doi:10.1007/s00024-008-0301-4, 2008.
- 413 Lund, M. G. and Austrheim, H.: High-pressure metamorphism and deep-crustal seismicity: evidence from
414 contemporaneous formation of pseudotachylytes and eclogite facies coronas, *Tectonophysics*, 372(1–2), 59–83,
415 doi:10.1016/S0040-1951(03)00232-4, 2003.
- 416 Maddock, R. H., Grocott, J. and Van Nes, M.: Vesicles, amygdales and similar structures in fault-generated
417 pseudotachylytes, *Lithos*, 20(5), 419–432, 1987.
- 418 Major, R. B. and Connor, C. H. H.: The Precambrian, in *The geology of South Australia*, vol. 1, edited by J. F. Drexel,
419 W. V. Preiss, and A. J. Parker, pp. 156–167, Geological Survey of South Australia., 1993.



- 420 Mancktelow, N. S. and Pennacchioni, G.: Why calcite can be stronger than quartz, *J. Geophys. Res.*, 115(B1),
421 doi:10.1029/2009JB006526, 2010.
- 422 McKenzie, D. and Brune, J. N.: Melting on fault planes during large earthquakes, *Geophys. J. Int.*, 29(1), 65–78, 1972.
- 423 Menegon, L., Nasipuri, P., Stünitz, H., Behrens, H. and Ravna, E.: Dry and strong quartz during deformation of the
424 lower crust in the presence of melt, *J. Geophys. Res.*, 116(B10), doi:10.1029/2011JB008371, 2011.
- 425 Mitra, S., Priestley, K., Bhattacharyya, A. K. and Gaur, V. K.: Crustal structure and earthquake focal depths beneath
426 northeastern India and southern Tibet: Crustal structure beneath NE India, *Geophys. J. Int.*, 160(1), 227–248,
427 doi:10.1111/j.1365-246X.2004.02470.x, 2004.
- 428 Moecher, D. P. and Steltenpohl, M. G.: Direct calculation of rupture depth for an exhumed paleoseismogenic fault
429 from mylonitic pseudotachylyte, *Geology*, 37(11), 999–1002, 2009.
- 430 Moecher, D. P. and Steltenpohl, M. G.: Petrological evidence for co-seismic slip in extending middle-lower
431 continental crust: Heier's zone of pseudotachylyte, north Norway, *Geol. Soc. Lond. Spec. Publ.*, 359(1), 169–186,
432 doi:10.1144/SP359.10, 2011.
- 433 Northern Territory Geological Survey, Edgoose, C. J., Close, D. F., Scrimgeour, I., Northern Territory and Department
434 of Mines and Energy: Australia 1:250 000 geological series. Sheet SG 52-7, Sheet SG 52-7, 1999.
- 435 Pennacchioni, G. and Cesare, B.: Ductile-brittle transition in pre-Alpine amphibolite facies mylonites during evolution
436 from water-present to water-deficient conditions (Mont Mary nappe, Italian Western Alps), *J. Metamorph. Geol.*,
437 15(6), 777–791, 1997.
- 438 Pittarello, L., Pennacchioni, G. and Di Toro, G.: Amphibolite-facies pseudotachylytes in Premosello metagabbro and
439 felsic mylonites (Ivrea Zone, Italy), *Tectonophysics*, 580, 43–57, doi:10.1016/j.tecto.2012.08.001, 2012.
- 440 Price, N. A., Johnson, S. E., Gerbi, C. C. and West, D. P.: Identifying deformed pseudotachylyte and its influence on
441 the strength and evolution of a crustal shear zone at the base of the seismogenic zone, *Tectonophysics*, 518–521, 63–
442 83, doi:10.1016/j.tecto.2011.11.011, 2012.
- 443 Rao, N. P., Tsukuda, T., Kosuga, M., Bhatia, S. C. and Suresh, G.: Deep lower crustal earthquakes in central India:
444 inferences from analysis of regional broadband data of the 1997 May 21, Jabalpur earthquake, *Geophys. J. Int.*, 148(1),
445 132–138, 2002.
- 446 Reyners, M., Eberhart-Phillips, D. and Stuart, G.: The role of fluids in lower-crustal earthquakes near continental rifts,
447 *Nature*, 446(7139), 1075–1078, doi:10.1038/nature05743, 2007.
- 448 Scharbert, P. D. H. G., Korkisch, P. D. J. and Steffan, D. I.: Uranium, thorium and potassium in granulite facies rocks,
449 Bohemian Massif, Lower Austria, Austria, *Tschemm's Mineral. Petrogr. Mitteilungen*, 23(4), 223–232,
450 doi:10.1007/BF01083102, 1976.
- 451 Sibson, R. H.: Generation of pseudotachylyte by ancient seismic faulting, *Geophys. J. Int.*, 43(3), 775–794, 1975.
- 452 Sibson, R. H.: Transient discontinuities in ductile shear zones, *J. Struct. Geol.*, 2(1), 165–171, 1980.
- 453 Sibson, R. H. and Toy, V. G.: The habitat of fault-generated pseudotachylyte: Presence vs. absence of friction-melt,
454 in *Geophysical Monograph Series*, vol. 170, edited by R. Abercrombie, A. McGarr, H. Kanamori, and G. Di Toro, pp.
455 153–166, American Geophysical Union, Washington, D. C. [online] Available from:
456 <http://www.agu.org/books/gm/v170/170GM16/170GM16.shtml> (Accessed 21 January 2014), 2006.
- 457 Singer, J., Diehl, T., Husen, S., Kissling, E. and Duretz, T.: Alpine lithosphere slab rollback causing lower crustal
458 seismicity in northern foreland, *Earth Planet. Sci. Lett.*, 397, 42–56, doi:10.1016/j.epsl.2014.04.002, 2014.



- 459 Smithies, R. H., Howard, H. M., Evins, P. M., Kirkland, C. L., Kelsey, D. E., Hand, M., Wingate, M. T. D., Collins,
460 A. S. and Belousova, E.: High-Temperature Granite Magmatism, Crust-Mantle Interaction and the Mesoproterozoic
461 Intracontinental Evolution of the Musgrave Province, Central Australia, *J. Petrol.*, 52(5), 931–958,
462 doi:10.1093/petrology/egr010, 2011.
- 463 Steltenpohl, M. G., Kassos, G. and Andresen, A.: Retrograded eclogite-facies pseudotachylytes as deep-crustal
464 paleoseismic faults within continental basement of Lofoten, north Norway, *Geosphere*, 2(1), 61–72,
465 doi:10.1130/GES00035.1, 2006.
- 466 Thielmann, M., Rozel, A., Kaus, B. J. P. and Ricard, Y.: Intermediate-depth earthquake generation and shear zone
467 formation caused by grain size reduction and shear heating, *Geology*, 43(9), 791–794, doi:10.1130/G36864.1, 2015.
- 468 Ueda, T., Obata, M., Di Toro, G., Kanagawa, K. and Ozawa, K.: Mantle earthquakes frozen in mylonitized ultramafic
469 pseudotachylytes of spinel-lherzolite facies, *Geology*, 36(8), 607, doi:10.1130/G24739A.1, 2008.
- 470 Wade, B. P., Barovich, K. M., Hand, M., Scrimgeour, I. R. and Close, D. F.: Evidence for early Mesoproterozoic arc
471 magmatism in the Musgrave Block, central Australia: implications for Proterozoic crustal growth and tectonic
472 reconstructions of Australia, *J. Geol.*, 114(1), 43–63, 2006.
- 473 Wenk, H. R.: Are pseudotachylites products of fracture or fusion?, *Geology*, 6(8), 507–511, doi:10.1130/0091-
474 7613(1978)6<507:APPOFO>2.0.CO;2, 1978.
- 475 Wex, S., Mancktelow, N. S., Hawemann, F., Camacho, A. and Pennacchioni, G.: Geometry of a large-scale, low-
476 angle, mid-crustal thrust (Woodroffe Thrust, central Australia): Geometry of a mid-crustal thrust, *Tectonics*,
477 doi:10.1002/2017TC004681, 2017.
- 478 White, J. C.: Transient discontinuities revisited: pseudotachylyte, plastic instability and the influence of low pore fluid
479 pressure on deformation processes in the mid-crust, *J. Struct. Geol.*, 18(12), 1471–1486, 1996.
- 480 White, J. C.: Instability and localization of deformation in lower crust granulites, Minas fault zone, Nova Scotia,
481 Canada, *Geol. Soc. Lond. Spec. Publ.*, 224(1), 25–37, doi:10.1144/GSL.SP.2004.224.01.03, 2004.
- 482 White, J. C.: Paradoxical pseudotachylyte – Fault melt outside the seismogenic zone, *J. Struct. Geol.*, 38, 11–20,
483 doi:10.1016/j.jsg.2011.11.016, 2012.
- 484 Whitney, D. L. and Evans, B. W.: Abbreviations for names of rock-forming minerals, *Am. Mineral.*, 95(1), 185–187,
485 doi:10.2138/am.2010.3371, 2010.
- 486 XU, Y., Roecker, S. W., WEI, R.-P., ZHANG, W.-L. and WEI, B.: Analysis of Seismic Activity in the Crust from
487 Earthquake Relocation in the Central Tien Shan, *Chin. J. Geophys.*, 48(6), 1388–1396, 2005.
- 488 Zhao, J., McCulloch, M. and Korsch, R. J.: Characterisation of a plume-related ~ 800 Ma magmatic event and its
489 implications for basin formation in central-southern Australia, *Earth Planet. Sci. Lett.*, 121, 349–367, 1994.
- 490